Determination of diffractive PDFs from a global QCD analysis of inclusive diffractive DIS and dijet cross-section measurements at HERA

Maral Salajegheh,[1,*] Hamzeh Khanpour,[2,3,4,5,†] Ulf-G. Meißner,[1,6,7,‡] Hadi Hashamipour,[5,§] and Maryam Soleymaninia[5,‖]

[1]*Helmholtz-Institut für Strahlen-und Kernphysik and Bethe Center for Theoretical Physics, Universität Bonn, D-53115 Bonn, Germany*
[2]*Dipartimento Politecnico di Ingegneria ed Architettura, University of Udine, Via della Scienze 206, 33100 Udine, Italy*
[3]*International Centre for Theoretical Physics (ICTP), Strada Costiera 11, 34151 Trieste, Italy*
[4]*Department of Physics, University of Science and Technology of Mazandaran, P.O. Box 48518-78195, Behshahr, Iran*
[5]*School of Particles and Accelerators, Institute for Research in Fundamental Sciences (IPM), P.O. Box 19395-5531, Tehran, Iran*
[6]*Institute for Advanced Simulation and Institut für Kernphysik, Forschungszentrum Jülich, D-52425 Jülich, Germany*
[7]*Tbilisi State University, 0186 Tbilisi, Georgia*

(Received 26 April 2023; accepted 8 May 2023; published 30 May 2023)

We present an updated set of SKMHS diffractive parton distribution functions (PDFs). In addition to the diffractive deep-inelastic scattering (diffractive DIS) datasets, the recent diffractive dijet cross-section measurement by the H1 experiment from the HERA collider are added to the data sample. The new set of diffractive PDFs, entitled SKMHS23 and SKMHS23-dijet, are presented at next-to-leading order (NLO) and next-to-next-to-leading order (NNLO) accuracy in perturbative QCD. Since the gluons directly contribute to jet production through the boson-gluon fusion process, the data on diffractive dijet production in inclusive DIS help constrain the gluon density, allowing for the determination of both the quark and gluon densities with better accuracy. The NLO and NNLO theory predictions calculated using both SKMHS23 and SKMHS23-dijet are compared to the analyzed data showing excellent agreement. The effect arising from the inclusion of diffractive dijet data and higher-order QCD corrections on the extracted diffractive PDFs and data/theory agreements are clearly examined and discussed.

DOI: 10.1103/PhysRevD.107.094038

I. INTRODUCTION

In the deep-inelastic scattering (DIS) process, the diffractive reactions of the type $ep \to eXY$, where X indicates a high-mass hadronic final state, represent about 8%–10% of the events at the Hadron-Electron Ring Accelerator (HERA), and Y stands for the forward system consisting of the leading proton. Such type of process provides rich experimental input to test quantum chromodynamics (QCD) in the diffractive regime [1–5].

According to the QCD factorization theorem [6,7], calculations of the diffractive cross sections with high enough Q^2 factorize into two main different parts: a set of diffractive parton distribution functions (PDFs) and a process-dependent hard scattering coefficient function.

The diffractive PDFs need to be determined from a QCD fit to the measured inclusive diffractive cross sections by applying the standard Dokshitzer-Gribov-Lipatov-Altarelli-Parisi (DGLAP) evolution equations [8–11], while the hard scattering coefficient functions are calculable in perturbative QCD. The QCD factorization is proven to hold both for the inclusive and the dijet diffractive processes [6,7]. However, in the case of low photon virtuality, some nonperturbative quantities such as higher twist effects need to be taken into account.

From an phenomenological point of view, the diffractive PDFs are determined by assuming an additional factorization that depends on the structure of a colorless exchange

*Maral@hiskp.uni-bonn.de
†Hamzeh.Khanpour@cern.ch
‡meissner@hiskp.uni-bonn.de
§H_Hashamipour@ipm.ir
‖Maryam_Soleymaninia@ipm.ir

object. This assumption is known as proton vertex factorization [3]. In a diffractive DIS process, the Pomeron and Reggeon flux factors in the proton are introduced, and for the case of diffractively exchanged objects the universal parton densities are assumed. Several measurements on the diffraction in DIS suggest the validity of the proton vertex factorization assumption in diffractive DIS [3]. Diffractive PDFs are universal quantities for all diffractive DIS reactions, with the hardness of the DIS process being ensured by the virtuality of the exchanged photon, Q^2 [3].

Nearly all recent progress in the extraction of diffractive PDFs stems from the widely used H1 and ZEUS diffractive DIS cross-section measurements. Over the past few years, some groups have reported their sets of diffractive PDFs with uncertainties, such as H1-2006-DPDF [4], ZEUS-2010-DPDF [5], GKG18 [12], HK19 [13], MMKG19 [14], and the most recent analysis by SKMHS22 [15]. Among these diffractive PDF determinations, the HK19 and SKMHS22 are performed up to next-to-next-to-leading order (NNLO) accuracy in perturbative QCD, while the former are limited to the next-to-leading order (NLO). The GKG18 and SKMHS22 are performed in the framework of `xFitter` [16] in order to achieve a reliable fit and estimate of the diffractive PDF uncertainties. In addition, GKG18, HK19, and SKMHS22 also analyzed the most recent H1/ZEUS combined diffractive DIS cross-section measurements.

Up to now, predictions for diffractive DIS, and in particular the diffractive dijet production, were performed at NLO and NNLO in QCD. ZEUS-2010-DPDF analyzed also the diffractive dijet production data at NLO [5], and most recently the predictions for the dijet production is provided at NNLO in Ref. [17].

In this paper, we present SKMHS23-dijet, a new determination of diffractive PDFs using the previous analyzed inclusive diffractive DIS measurements by the H1 and ZEUS Collaborations, including for the first time the dijet production cross-section measurements in diffractive ep scattering data collected in the years 2005–2007 with the H1 detector at HERA. The SKMHS23-dijet is extracted from QCD analysis at NLO and NNLO accuracy in perturbative QCD. In order to analyze the dijet production data, the well-established `ALpos` framework [18–20] supplemented with APFEL [21] and `fastNLO` [22,23] is used, which is an object-oriented data to theory comparison fitting tool. The statistical analysis of the theory predictions for both diffractive DIS and dijet production are also performed using this program. The diffractive dijet production data that are included in SKMHS23-dijet help to constrain the gluon density, allowing for a good accuracy determination of both the quark and gluon densities. In order to examine the effect of dijet data on the extracted densities, we also present the SKMHS23 analysis in which the dijet data are excluded from the data sample. Finally, the NLO and NNLO theory predictions are compared to the analyzed data. The effect arising from the inclusion of diffractive dijet data and higher-order QCD corrections on the extracted diffractive PDFs and data/theory agreement is also examined and discussed.

The rest of the paper is organized as follows. The theoretical framework considered in SKMHS23-dijet is introduced in Sec. II. This section also discusses the QCD prediction for the diffractive dijet production in an electron-proton (ep) scattering process and the corresponding factorization theorem. The details of the SKMHS23 are presented in Sec. III, which includes the experimental input, the SKMHS23 parametrizations, the heavy quark contributors to the diffractive DIS process, and finally the fitting framework and minimization strategy. The SKMHS23 fit results and main findings of this work are scrutinized and discussed in Sec. IV. Finally, Sec. V summarizes the findings and outlines possible future developments as well.

II. THEORETICAL FRAMEWORK

In this section, we describe in detail the standard theoretical framework for diffractive DIS processes in which the perturbative QCD framework is applied for the event with a large rapidity gap (LRG) in the rapidity distribution of the outgoing hadrons. We thoroughly discuss the calculation of diffractive dijet cross sections in inclusive DIS processes as well and the relevant factorization theorem. We also provide the details of the factorization of the proton diffractive PDFs.

A. QCD prediction for diffractive dijet production in (ep) scattering

The diffraction $\gamma^* + p \to X + p$ in the single diffractive process, such as inclusive diffractive DIS $e(k) + p(P) \to e(k') + p(P') + X$, is observed when the virtual photon γ^* dissociates into the hadronic system X whereas the proton remains intact. The diffractive reaction in DIS is described by the DIS kinematic invariants which are given by

$$\begin{aligned} Q^2 &= -q^2 = (k - k'^2), \\ x &= \frac{-q^2}{2P \cdot q}, \\ y &= \frac{P \cdot q}{P \cdot k}, \end{aligned} \tag{1}$$

where Q^2 is the virtuality of the photon, x is the longitudinal fraction of the proton momentum carried by the struck quark (same as the Bjorken scaling variable), and y indicates the inelasticity. These quantities are related via $Q^2 = xys$, where the electron-proton center-of-mass energy squared is denoted by s.

In addition, the new quantities for diffractive kinematics are defined in relation to the scattered protons. One of them is the longitudinal momentum fraction of the exchanged Pomeron,

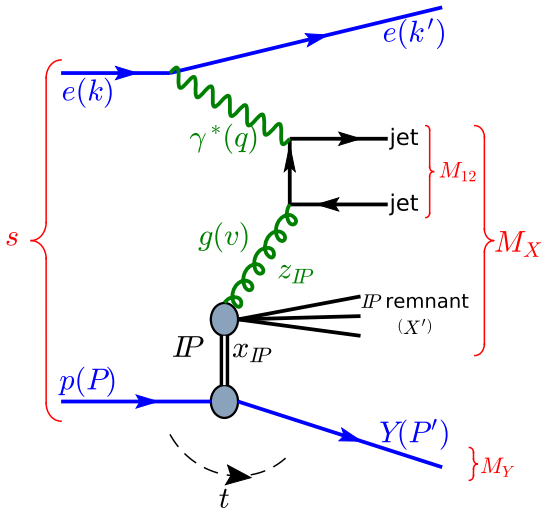

FIG. 1. The Feynman diagram describing the diffractive dijet production in an electron-proton collision at HERA.

$$x_{\mathbb{P}} = \frac{q \cdot (P - P')}{q \cdot P}. \tag{2}$$

The second variable is the squared four-momentum transfer at the proton vertex,

$$t = (P' - P)^2. \tag{3}$$

Finally, the last one is the fractional momentum of the diffractive exchange carried by the parton inside the Pomeron,

$$\beta = \frac{x}{x_{\mathbb{P}}} = \frac{Q^2}{2q \cdot (P - P')}. \tag{4}$$

The cross section of diffractive dijet (jj) production $e + p \to e + p + jj + X'$ is an important observable which can affect the behavior of diffractive PDFs. The inclusion of these data in the analysis is one of the main objectives of this study. The Feynman diagram describing the diffractive dijet production in an electron-proton collision at HERA is shown in Fig. 1. For the diffractive dijet production, an additional variable needs to be introduced. According to the Feynman diagram presented in Fig. 1, in the hard subprocess, v is the four-momentum of the gluon emitted from the Pomeron.

The longitudinal momentum fraction of the gluon is denoted by $z_{\mathbb{P}}$, the new invariant,

$$z_{\mathbb{P}} = \frac{q \cdot v}{q \cdot (P - P')}. \tag{5}$$

It should be noted here that for the dijet production process the variable x is not the momentum fraction of the parton entering to the hard subprocess. This fraction is denoted as $\tilde{x}$ and it is the momentum fraction of the interacting parton with respect to the proton. Further, $x_{\mathbb{P}}$ is the momentum fraction of the Pomeron with respect to the proton. The momentum fraction of the parton with respect to the Pomeron is denoted by $z_{\mathbb{P}}$. It can be shown that for the dijet production one can write,

$$z_{\mathbb{P}} = \frac{\tilde{x}}{x_{\mathbb{P}}}. \tag{6}$$

At leading order (LO), the center-of-mass energy of the hard subprocess is equal to the invariant mass of the dijet system M_{12},

$$M_{12}^2 = (q + v)^2. \tag{7}$$

In the next section, the factorization theorem will be presented and discussed.

B. Factorization theorem in diffractive dijet production

The factorization theorem of QCD can be employed for the diffractive processes so that the cross section of dijet production is given by the convolution of diffractive PDFs for proton $f^D_{i/p}$ with the partonic cross sections $d\hat{\sigma}$ [6,7],

$$\begin{aligned} d\sigma(e + p \to e + p + jj + X') &= \sum_i \int dt \int dx_{\mathbb{P}} \int dz_{\mathbb{P}} \\ &\times f^D_{i/p}(z_{\mathbb{P}}, \mu_F^2, x_{\mathbb{P}}, t) \otimes d\hat{\sigma}_{ei \to jj}(\hat{s}, \mu_R^2, \mu_F^2). \end{aligned} \tag{8}$$

Here, the hadronic system X' is what remains of the hadronic system X after removing the two jets. In addition, the integrals are performed over the accepted phase space and the sum runs over all the partons contributing to the cross section. The first argument of the diffractive PDFs $f^D_{i/p}$ is the momentum of the parton with respect to the Pomeron. μ_F and μ_R represent the factorization and renormalization scales, respectively. The invariant energy squared in the subprocess is defined as

$$\bar{s} \sim x_{\mathbb{P}} z_{\mathbb{P}} y s - Q^2. \tag{9}$$

In the DIS region in which $Q^2 \gg \Lambda^2$, the only relevant contribution to the dijet production cross section is the direct process defined in Eq. (8).

According to the proton vertex factorization theorem, the diffractive PDFs can be factorized into the product of two distinct terms. The first term depends on the $x_{\mathbb{P}}$ and t, while the second term depends only on the $z_{\mathbb{P}}$ and μ_F. Hence, the diffractive PDFs $f^D_{i/p}(z_{\mathbb{P}}, \mu_F^2; x_{\mathbb{P}}, t)$ is given by

$$\begin{aligned} f^D_{i/p}(z_{\mathbb{P}}, \mu_F^2; x_{\mathbb{P}}, t) &= f_{\mathbb{P}/p}(x_{\mathbb{P}}, t) f_{i/\mathbb{P}}(z_{\mathbb{P}}, \mu_F^2) \\ &+ n_{\mathbb{R}} f_{\mathbb{R}/p}(x_{\mathbb{P}}, t) f_{i/\mathbb{R}}(z_{\mathbb{P}}, \mu_F^2), \end{aligned} \tag{10}$$

where the Pomeron and Reggeon flux factors are denoted by $f_{\mathbb{P}/p}(x_{\mathbb{P}}, t)$ and $f_{\mathbb{R}/p}(x_{\mathbb{P}}, t)$, respectively. The flux factors describe the emission of the Pomeron and Reggeon from the proton target. The Reggeon contributes significantly at low $z_{\mathbb{P}}$ and large $x_{\mathbb{P}}$. The global normalization of the Reggeon contribution is $n_{\mathbb{R}}$, which is taken as a free parameter in the fit. The Pomeron and Reggeon partonic distribution functions are indicated by $f_{i/\mathbb{P}}(z_{\mathbb{P}}, \mu_F^2)$ and $f_{i/\mathbb{R}}(z_{\mathbb{P}}, \mu_F^2)$, respectively.

The parametrization and determination of these distribution functions will be discussed in detail in Sec. III B.

Many properties of diffractive PDFs are similar to the nondiffractive PDFs. Despite the fact that the presence of the leading proton in the final state leads to an additional constraint for the calculation of diffractive PDFs, they still obey the standard DGLAP evolution equation like the ordinary PDFs [8–11]. In the analysis of diffractive PDFs the cross section for diffractive processes has a t dependence, which one usually integrates out. Consequently, the t dependence of diffractive PDFs is restricted to $|t| < 1.0$ GeV^2 here.

As mentioned before, our aim in this paper is to include the dijet production cross section in the diffractive DIS analysis up to NNLO. The calculations of partonic cross sections of diffractive dijet production at NNLO accuracy and the one from dijet production in DIS are the same. Recently, the latter calculations have been used to describe the inclusive dijet cross section in DIS [24,25].

For the PDFs evolution and to compute the inclusive DIS cross sections at NLO and NNLO accuracy, we use publicly available APFEL package [21]. According to Eq. (8), to calculate the diffractive dijet cross section one needs to convolute the partonic cross section $d\hat{\sigma}_{ei\to jj}$ with the diffractive PDFs $f^D_{i/p}(z_{\mathbb{P}}, \mu_F^2, x_{\mathbb{P}}, t)$. In our work, the hard (partonic) cross section at NLO accuracy is calculated using the NLOJET++ package [26], however, to account for the additional dependence of the cross section on $x_{\mathbb{P}}$ and t some adjustments are required as specified in Ref. [17]. To compute the NNLO corrections to dijet partonic cross sections, one can use the NNLOJET [17,27]. This calculation can be very time consuming using conventional methods such as Monte Carlo integration, especially if one requests a high precision. Nevertheless, in a QCD analysis one should repeatedly evaluate this convolution for different values of diffractive PDF parameters. To overcome this difficulty, an interface to the fastNLO package is implemented in the ALPOS framework [18–20] to perform the QCD fit. By using the methodology of the fastNLO, the calculation of matrix elements is done only once and the convolution integral turns into a summation over a grid of integration variables [22]. Additional information and details of the fastNLO formalism can be found in, e.g., [28].

III. DETAILS OF THE SKMHS23 QCD ANALYSIS

In this section, we present the details of the SKMHS23 QCD analysis, including the experimental datasets analyzed in this work, the diffractive PDFs parametrization, the minimization procedures, and the diffractive PDF uncertainty method.

A. Experimental datasets

This section deals with the experimental datasets used in the SKMHS23 global QCD analysis, focusing on the diffractive dijet cross-section measurements at HERA. The details of the inclusive diffractive DIS experimental input are discussed in detail in our previous studies [12,15] and we will present a short review here.

The determination of diffractive PDFs relies mainly on the inclusive diffractive DIS cross-section measurements by the H1 and ZEUS Collaborations. The inclusive diffractive DIS and dijet datasets which are listed in Tables I and II include the following:

(i) The H1 measurements of the inclusive diffractive DIS cross section H1-LRG-11 at the $\sqrt{s} = 225, 252, 319$ GeV^2 which covers the phase space of $4.0 < Q^2 < 44.0$ GeV^2 and $5.0 \times 10^{-4} < x_{\mathbb{P}} < 3.0 \times 10^{-3}$ [29].

(ii) The inclusive measurement of diffractive DIS by the H1 Collaboration, called H1-LRG-12 [30]. This measurement covers the phase space $3.0 < Q^2 < 1600$ GeV^2 of the photon virtuality and the squared four-momentum transfer of $|t| < 1.0$ GeV^2.

(iii) The most recent published data on the diffractive DIS cross section come from the H1 and ZEUS combined measurement which is useful to determine precise diffractive PDFs with reliable uncertainty. The kinematic range of these measurements is $2.5 < Q^2 < 200$ GeV^2 for the photon virtuality, $3.5 \times 10^{-4} < x_{\mathbb{P}} < 9.0 \times 10^{-2}$ for the proton fractional momentum loss, $1.8 \times 10^{-3} < \beta < 0.816$ in scaled fractional momentum variable, and finally $0.09 < |t| < 0.55$ GeV^2 in the squared four-momentum transfer at the proton vertex [31].

As discussed in detail in Refs. [12,13], the H1 and ZEUS combined data are subject to two different corrections which are the proton dissociation background and the global normalization factor for the extrapolation from $0.09 < |t| < 0.55$ to $|t| < 1.0$ GeV^2.

(iv) The recent differential dijet cross-section measurements in diffractive DIS published by the H1 Collaboration at HERA which correspond to an integrated luminosity of 290 pb^{-1} [32]. The phase space of these measurements is spanned by the photon virtuality of $4.0 < Q^2 < 100$ GeV^2 and by the fractional proton longitudinal momentum loss $x_{\mathbb{P}} < 3.0 \times 10^{-2}$. As will be discussed in detail

TABLE I. List of all diffractive DIS data points with their properties used in the SKMHS23 global QCD analysis. For each dataset we provide the kinematical coverage of β, $x_{\mathbb{P}}$, and Q^2. The number of data points is displayed as well. The details of the kinematical cuts applied on these datasets are explained in the text.

Experiment	Observable	$[\beta^{\min}, \beta^{\max}]$	$[x_{\mathbb{P}}{}^{\min}, x_{\mathbb{P}}{}^{\max}]$	Q^2 [GeV^2]	Number of points	Reference
H1-LRG-11 $\sqrt{s} = 225$ GeV	$\sigma_r^{D(3)}$	[0.033–0.88]	$[5\times10^{-4} - 3\times10^{-3}]$	4–44	22	[29]
H1-LRG-11 $\sqrt{s} = 252$ GeV	$\sigma_r^{D(3)}$	[0.033–0.88]	$[5\times10^{-4} - 3\times10^{-3}]$	4–44	21	[29]
H1-LRG-11 $\sqrt{s} = 319$ GeV	$\sigma_r^{D(3)}$	[0.089–0.88]	$[5\times10^{-4} - 3\times10^{-3}]$	11.5–44	14	[29]
H1-LRG-12	$\sigma_r^{D(3)}$	[0.0017–0.80]	$[3\times10^{-4} - 3\times10^{-2}]$	3.5–1600	277	[30]
H1/ZEUS combined	$\sigma_r^{D(3)}$	[0.0018–0.816]	$[3\times10^{-4} - 9\times10^{-2}]$	2.5–200	192	[31]
Total data					526	

TABLE II. Dijet dataset used in the SKMHS23-dijet global QCD analysis.

Experiment	Observable	DIS range	Dijet range	Diffractive range	Number of points	Reference
H1-LRG (HERA II)	$d^2\sigma/dp_T^{*\text{jet1}}dQ^2$	$0.1 < y < 0.7$ $4 < Q^2 < 100$ GeV^2	$p_T^{*\text{jet1}} > 5.5$ GeV $p_T^{*\text{jet2}} > 4.0$ GeV $-1 < \eta^{\text{jet}} < 2$	$x_{\mathbb{P}} < 0.03$ $\lvert t\rvert < 1$ GeV^2 $M_Y < 1.6$ GeV	15	[32]
Total data					15	

below, the diffractive DIS dijet data are used in the SKMHS23 QCD analysis for the first time. The effect arising from the inclusion of these data on the extracted diffractive PDFs and data/theory agreements will also be discussed. It is worth noting here that there are some other dijet cross-section measurements [33–37] that we plan to consider and analyze in terms of future work.

Finally, in order to avoid the contributions from higher twist and some other nonperturbative effects, one needs to implement some kinematical cuts to all diffractive DID datasets mentioned above. To this end, we follow the formalism presented in Refs. [5,12,15] and consider some cuts on the data samples. We consider $M_X \geq 2$ GeV, the datasets for $\beta \geq 0.81$ are excluded. A χ^2 scan is performed in Ref. [12] to find an optimum value for the Q^2. In this work, the region with $Q^2 = Q^2_{\min} \geq 9$ GeV^2 only is included in the fit, which shows the best data/theory description.

B. SKMHS23 diffractive PDFs parametrization

Like the standard PDFs, the diffractive PDFs are nonperturbative quantities and should be determined by a QCD global analysis. As it has been mentioned before, diffractive PDFs are the sum of Pomeron and secondary Reggeon contributions neglecting the possible interference terms. We consider the parametrization form for diffractive PDFs with unknown parameters at a starting scale $\mu_0^2 = 1.69$ GeV^2, which is less than the squared charm mass (m_c^2) threshold.

Due to the lack of experimental data for the case of diffractive processes, a somewhat less flexible parametrization form for the diffractive PDFs is employed in our work. For the same reason the Pomeron PDFs at the initial scale $f_{i/\mathbb{P}}(z_{\mathbb{P}}, \mu_0^2)$ should be the same for all light partons $i = u = d = s = \bar{u} = \bar{d} = \bar{s}$, while the gluon distribution is considered separately. The contribution of the Reggeon PDFs becomes important at large values of $x_{\mathbb{P}}$ and it is equal to the pion PDF. For the leading Pomeron pole at starting scale Q_0^2, we parametrize the input gluon and quark-singlet diffractive PDFs as follows:

$$zf_{g/\mathbb{P}}(z, Q_0^2) = \alpha_g z^{\beta_g}(1-z)^{\gamma_g}(1+\eta_g\sqrt{z}), \quad (11)$$

$$zf_{q/\mathbb{P}}(z, Q_0^2) = \alpha_q z^{\beta_q}(1-z)^{\gamma_q}(1+\eta_q\sqrt{z}). \quad (12)$$

The longitudinal momentum fraction z at the lowest order of the hard process is equal to β ($z = \beta$), then by including the higher orders we have $0 < \beta < z$. To ensure that the diffractive PDFs vanish at $z = 1$, the above equations are multiplied by factor $e^{\frac{-0.01}{1-z}}$, which is required for the DGLAP equations to be solvable [4,5]. The $x_{\mathbb{P}}$ dependence of the diffractive PDFs is then determined by Pomeron and Reggeon flux factors which are parametrized such that,

$$f_{\mathbb{P}/p,\mathbb{R}/p}(x_{\mathbb{P}}, t) = A_{\mathbb{P},\mathbb{R}} \frac{e^{B_{\mathbb{P},\mathbb{R}}t}}{x_{\mathbb{P}}^{2\alpha_{\mathbb{P},\mathbb{R}}(t)-1}}. \quad (13)$$

We assume linear trajectories of the form

$$\alpha_{\mathbb{P},\mathbb{R}}(t) = \alpha_{\mathbb{P},\mathbb{R}}(0) + \alpha'_{\mathbb{P},\mathbb{R}} t. \tag{14}$$

Further, $A_{\mathbb{P},\mathbb{R}}$ are the normalizations of the Pomeron and Reggeon terms, respectively, and are treated in the same way as in Ref. [4].

After assessing the fits using Eqs. (11) and (12), we found that the parameters η_q and η_g cannot be well constrained by the diffractive data, therefore, we set them to zero. In Eqs. (13) and (14), we set the Reggeon flux parameters to the same value as in [4,37]. For the Pomeron flux parameters $\alpha'_{\mathbb{P}}$ and $B_{\mathbb{P}}$ we use the latest value from Ref. [38] and leave $\alpha_{\mathbb{P}}(0)$ to be free. It needs to be determined from the QCD fit. Therefore, in total we have eight free parameters α_q, β_q, γ_q, α_g, β_g, γ_g, $n_{\mathbb{R}}$, and $\alpha_{\mathbb{P}}(0)$. These will be determined from the fit to the experimental data. For the initial inputs, we adopt the world average value for $\alpha_s^{n_f=5}(M_Z^2) = 0.1185$ [39], and the charm and bottom masses are set to $m_c = 1.40$ and $m_b = 4.50$ GeV for both NLO and NNLO accuracy.

The heavy flavors will be generated through the evolution equations at $Q^2 > m_{c,b}^2$. For the contribution of the heavy flavors in diffractive DIS, we employ the FONLL scheme implemented in the APFEL package [21]. The FONLL is a general-mass variable flavor number scheme (GM-VFNS) and the abbreviation stands for "fixed-order plus next-to-leading log orders." This approach introduced first in Ref. [40] to investigate the production of heavy quarks in hadroproduction, then extended to DIS [41] and also to Higgs boson production [42]. This method is used to combine a fixed-order calculation which corresponds to the massive $\mathcal{O}(\alpha^3)$ cross section with a next-to-leading log resummed computation of cross section in the massless limit. For more details, we refer the reader to Ref. [40] and references therein. In the SKMHS23 QCD analysis, we choose the FONLL-B scheme at NLO accuracy which is expected to be more accurate to describe the small-$x_{\mathbb{P}}$ data points [43], while for the case of NNLO, the FONLL-C is considered. More details of these schemes can be found in Ref. [44].

C. Minimization and diffractive PDF uncertainty method

As already discussed, the SKMHS23 QCD analysis of the diffractive PDFs is presented at NLO and NNLO in perturbative QCD with as much data as possible. As a phenomenological study of diffractive PDFs, the SKMHS23 analysis should answer three questions adequately: 1) how to adjust the free fit parameters of the model, 2) how to predict observables precisely, and 3) how precise are our distributions and observable predictions. As mentioned, a QCD analysis should have a sound approach to finding the best fit parameters and evaluate their uncertainty. In order to find the best values of the free parameters, a χ^2 function defined as follows, is minimized [45]:

$$\chi^2 = \vec{p}^{\,\mathrm{T}} \mathbf{C}^{-1} \vec{p} + \sum_k^{N_{\mathrm{sys}}} \varepsilon_k^2, \tag{15}$$

where $\mathbf{C}$ denotes the covariance matrix of the relative uncertainties, and the ith element of $\vec{p}$ is defined as the logarithm of the ratio of a measured observable to its theoretical prediction,

$$p_i = \log\left[\frac{\mathcal{E}_i}{\mathcal{T}_i}\right] - \sum_k^{N_{\mathrm{sys}}} E_{i,k}, \tag{16}$$

which means that the experimental data are distributed according to the log-normal distribution and where $E_{i,k}$ is defined as

$$E_{i,k} = \sqrt{f_k^C}\left(\frac{\delta_{\mathcal{E}_i}^{k,+} - \delta_{\mathcal{E}_i}^{k,-}}{2}\varepsilon_k + \frac{\delta_{\mathcal{E}_i}^{k,+} + \delta_{\mathcal{E}_i}^{k,-}}{2}\varepsilon_k^2\right). \tag{17}$$

The parameter f_k^C denotes the fraction of the systematic errors from the source k which are considered as correlated uncertainty and the parameters $\delta_{\mathcal{E}_i}^{k,-}$ and $\delta_{\mathcal{E}_i}^{k,+}$ are the relative uncertainty of the $\mathcal{E}_i$ measurement. The nuisance parameters ε_k will be treated as free parameters and will be determined by the χ^2 minimization.

Concerning the question of calculating the observables and evolution of the diffractive PDFs, we have used the ALPOS package [19,20], which also provides an interface to the CERN MINUIT package [46] that is responsible for the χ^2 minimization. For the uncertainty of diffractive PDF distributions and theoretical predictions, we have used the well established optimized Hessian method as described in [47] and implemented in the ALPOS package. In the next section we will discuss in detail the χ^2 values extracted from SKMHS23 QCD fits and the resulting diffractive PDFs in terms of their predictions and uncertainties.

IV. SKMHS23 FIT RESULTS

This section focuses on the main results of the SKMHS23 QCD analysis and on the new features and improvements that are introduced in this work. We first present the SKMHS23 diffractive PDFs and the fitted parameters. Then, we focus on the improvements arising from the inclusion of the higher-order QCD correction. We also stress and discuss the effect and impact of the diffractive dijet production data on the extracted diffractive PDFs. Finally, we present and discuss the quality of the SKMHS23 QCD fit in terms of both individual and total datasets. Data theory comparisons will be presented as well.

In Table III we present the SKMHS23 best fit parameters and their errors extracted from the QCD analysis at NLO and NNLO accuracy using the inclusive diffractive DIS data. The best fit parameters extracted from the global QCD

TABLE III. The SKMHS23 best fit parameters and their errors extracted from the QCD analysis at NLO and NNLO accuracy using the inclusive diffractive DIS data. Values marked with * are fixed in the QCD fit since the analyzed datasets do not constrain these parameters well enough. The input values for α_s, m_c, and m_b are also given.

Parameters	SKMHS23 (NLO)	SKMHS23 (NNLO)
α_g	0.355 ± 0.084	0.497 ± 0.108
β_g	0.201 ± 0.101	0.291 ± 0.087
γ_g	0.018 ± 0.206	0.353 ± 0.233
η_g	0.0*	0.0*
α_q	0.728 ± 0.055	0.979 ± 0.091
β_q	1.525 ± 0.071	1.705 ± 0.096
γ_q	0.437 ± 0.036	0.558 ± 0.044
η_q	0.0*	0.0*
$\alpha_{\mathbb{P}}(0)$	1.099 ± 0.004	1.010 ± 0.004
$n_{\mathbb{R}}$	0.00055 ± 0.000004	0.00055 ± 0.000004
$\alpha_s(M_Z^2)$	0.1185*	0.1185*
m_c (GeV)	1.40*	1.40*
m_b (GeV)	4.5*	4.5*

TABLE IV. The SKMHS23-dijet best fit parameters and their errors extracted from global the QCD analysis at NLO and NNLO accuracy using both inclusive diffractive DIS and diffractive dijet datasets. Values marked with * are fixed in the QCD fit since the analyzed datasets do not constrain these parameters well enough. The input values for α_s, m_c, and m_b are also given.

Parameters	SKMHS23-dijet (NLO)	SKMHS23-dijet (NNLO)
α_g	0.323 ± 0.069	0.477 ± 0.094
β_g	0.169 ± 0.094	0.278 ± 0.083
γ_g	-0.099 ± 0.163	0.303 ± 0.189
η_g	0.0*	0.0*
α_q	0.747 ± 0.055	0.986 ± 0.085
β_q	1.560 ± 0.068	1.719 ± 0.085
γ_q	0.442 ± 0.036	0.560 ± 0.043
η_q	0.0*	0.0*
$\alpha_{\mathbb{P}}(0)$	1.100 ± 0.003	1.101 ± 0.004
$n_{\mathbb{R}}$	0.00075 ± 0.000004	0.00073 ± 0.000004
$\alpha_s(M_Z^2)$	0.1185*	0.1185*
m_c (GeV)	1.40*	1.40*
m_b (GeV)	4.5*	4.5*

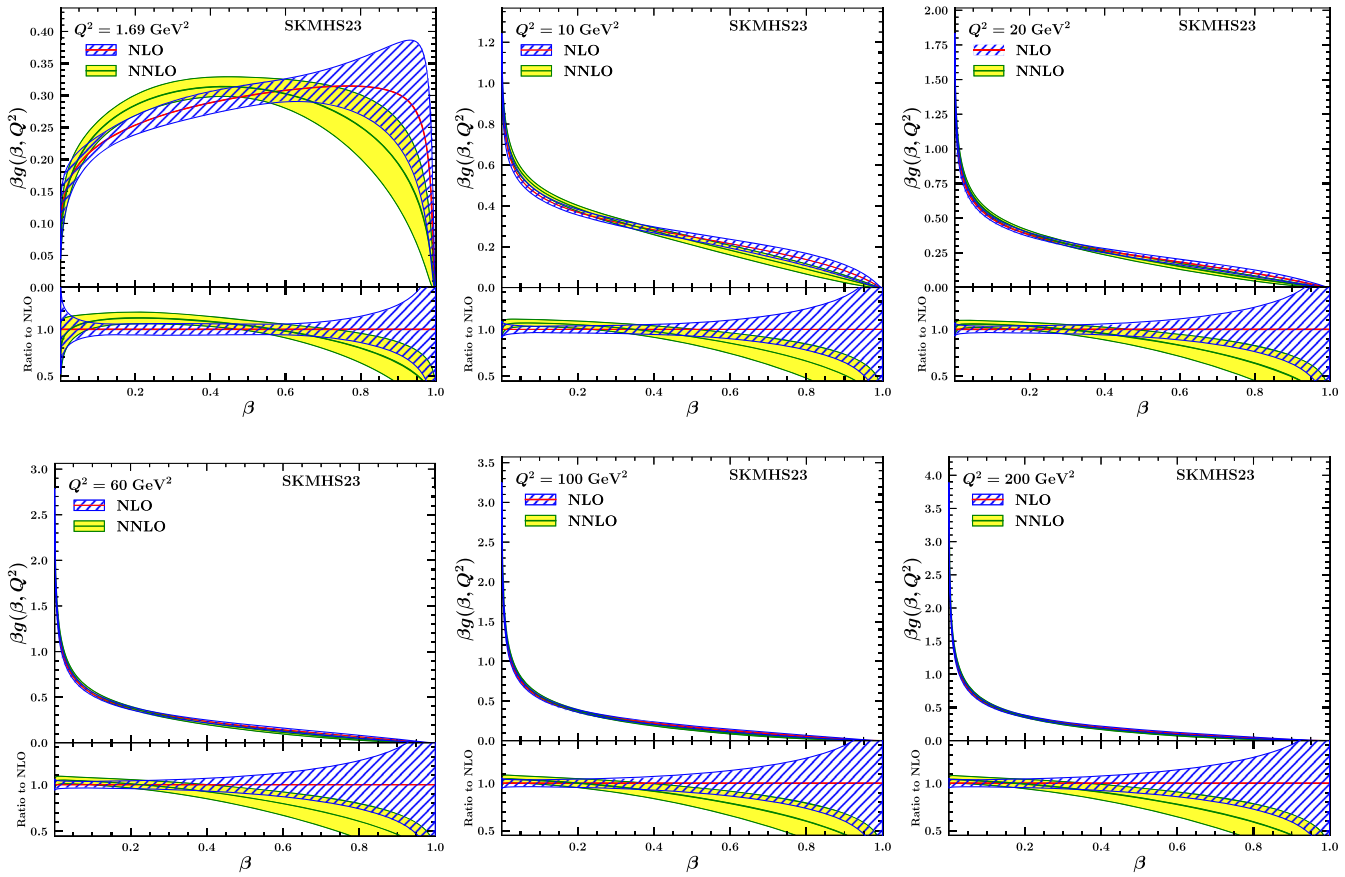

FIG. 2. The SKMHS23 gluon distribution at the input scale $Q_0^2 = 1.69$ GeV^2 and at higher energy values of 10, 20, 60, 100, and 200 GeV^2. The extracted uncertainties determined using the Hessian method also are shown. We show both the absolute distributions and ratios to the NLO results.

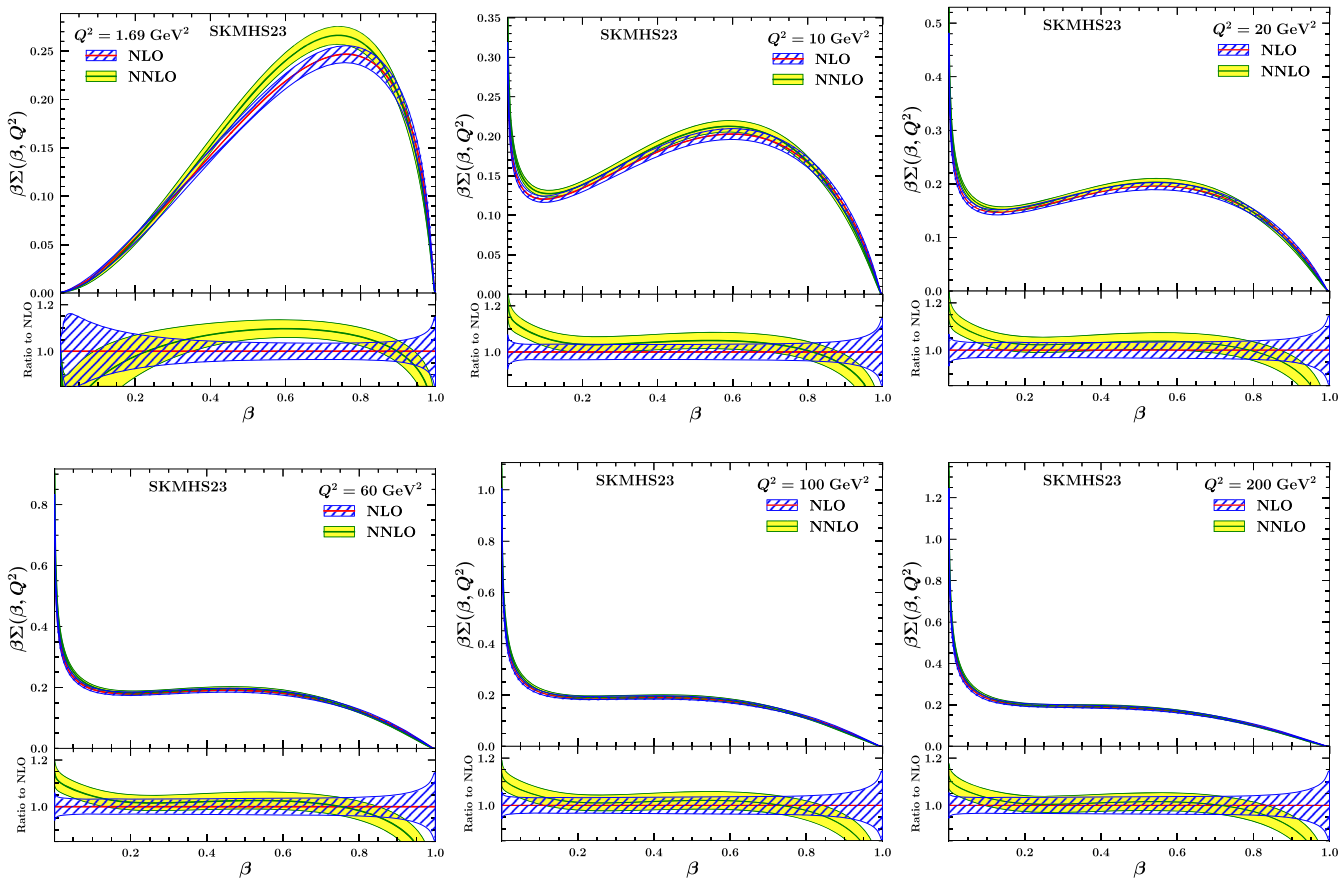

FIG. 3. Same as Fig. 2 but this time for the SKMHS23 singlet distribution with their included uncertainties.

analysis at NLO and NNLO accuracy using both inclusive diffractive DIS and diffractive dijet datasets, entitled SKMHS23-dijet, are presented in Table IV.

In total we have ten parameters that need to be extracted from the QCD fit, which include four for both the gluon and total singlet densities and two for the Reggeon flux. For both gluon and singlet PDFs, the parameters η_g and η_q are set to zero during the QCD fits since the analyzed datasets do not constrain these parameters well enough. As one can see from Tables III and IV, all the shape parameters are well determined, except for the case of γ_g which comes with large errors. This again reflects the lack of data to constrain all shape parameters. We prefer to keep γ_g free in the fit to give the gluon density enough flexibility. The extracted value for the $n_{\mathbb{R}}$ is rather small as expected [12]. The consistency of the parameters extracted from different QCD fits presented in Tables III and IV are acceptable, i.e., they describe the data rather well, however, the γ_g is mostly affected by the higher-order QCD corrections and the dijet data as well.

Now we are in a position to present and discuss the SKMHS23 and SKMHS23-dijet diffractive PDFs and their uncertainties, focusing on the perturbative convergence upon inclusion of the higher-order QCD corrections and the effect arising from the inclusion of the diffractive dijet production to the data sample.

In Fig. 2, we present the NLO and NNLO SKMHS23 gluon distributions at the input scale $Q_0^2 = 1.69$ GeV^2. The results for the higher energy values of 10, 20, 60, 100, and 200 GeV^2 are also shown. The extracted uncertainties determined using the Hessian method also are shown. We show both the absolute distributions and ratios to the NLO results. The NLO and NNLO SKMHS23 singlet distribution with their included uncertainties are shown in Fig. 3.

Considering the results presented in Figs. 2 and 3, a few remarks are in order. One can see that the difference between NLO and NNLO distributions is not substantial; we consider this property as a hint of perturbative convergence of the analysis. As one can see, a difference can be seen between the NLO and NNLO results for both the gluon and the singlet densities for medium to large values of β. For the gluon density, the NLO results are larger than the NNLO ones for a high value of β and smaller for the small region of β. As can be seen, a significant reduction for the uncertainty bands are achieved after including the higher-order QCD corrections showing the effect of the inclusion the NNLO accuracy in the diffractive PDFs

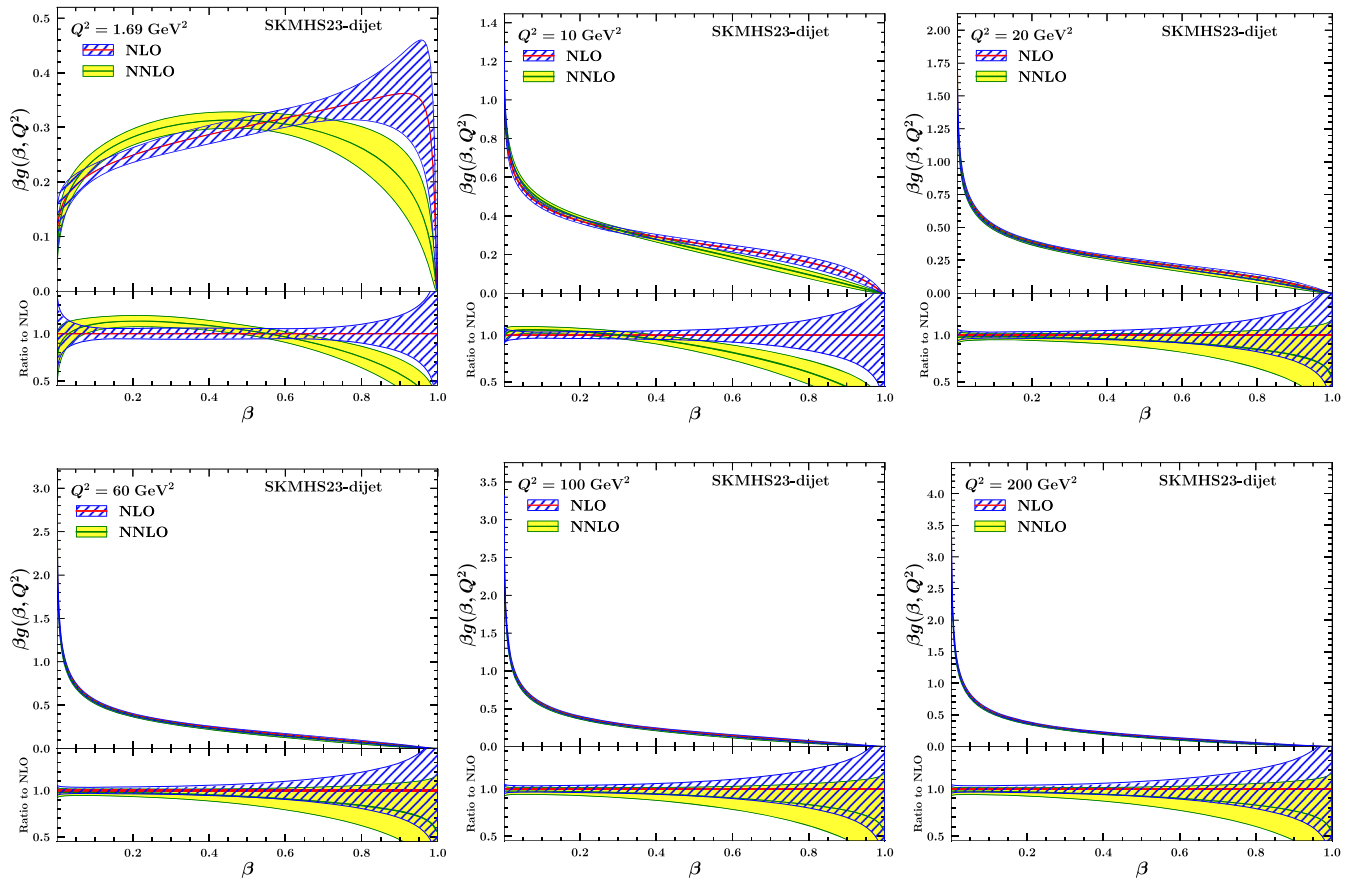

FIG. 4. The SKMHS23-dijet gluon distribution at the input scale $Q_0^2 = 1.69$ GeV^2 and at higher energy values of 10, 20, 60, 100, and 200 GeV^2. The extracted uncertainties determined using the Hessian method also are shown. We show both the absolute distributions and ratios to the NLO results.

determination. The differences between the NLO and NNLO diffractive PDFs are rather small when going to the higher values of Q^2.

In Figs. 4 and 5, we show the NLO and NNLO SKMHS23-dijet gluon and singlet distributions with their uncertainties determined using the Hessian method at the input scale $Q_0^2 = 1.69$ GeV^2. The results for the higher energy values of 10, 20, 60, 100, and 200 GeV^2 are also shown. We show both the absolute distributions and ratios to the NLO results. The same findings as in the case of the SKMHS23 also hold for the SKMHS23-dijet. A significant reduction for the uncertainty bands can bee seen at NNLO accuracy, mostly for large values of β.

In order to further scrutinize the results presented in this work and to examine the effect arising from the inclusion of the inclusive DIS dijet production data on the extracted diffractive PDFs, we present a comparison of the NLO and NNLO results for the SKMHS23 and SKMHS23-dijet in Fig. 6 at $Q_0^2 = 1.69$ GeV^2 for the gluon and singlet distributions. The upper panel of each plot displays the absolute distributions, while the lower panel displays the SKMHS23/SKMHS23-dijet ratios. As one can see, the inclusion of the dijet data mostly affects the shape of the gluon distribution for large values of β. It also affects the uncertainty bands of the extracted diffractive PDFs. It causes a reduction of the error bands for the gluon density at large values of β and for small values of β for the case of the total singlet density.

In Tables V and VI we present the values of the χ^2 per data point for both the individual and the total inclusive diffractive datasets included in the our analysis. The values for the SKMHS23 QCD fit are presented in Table V, and the values for our SKMHS23-dijet global QCD fit which includes the inclusive diffractive dijet production are presented in Table VI. The values are shown at NLO and NNLO for all the QCD analyses.

Concerning the fit quality of the total dataset, the most noticeable feature of the SKMHS23 and SKMHS23-dijet analyses is the slight improvement upon the inclusion of the higher-order corrections. Such kind of improvement also can be achieved after including the inclusive diffractive dijet production data in the QCD fit. As one can see, the

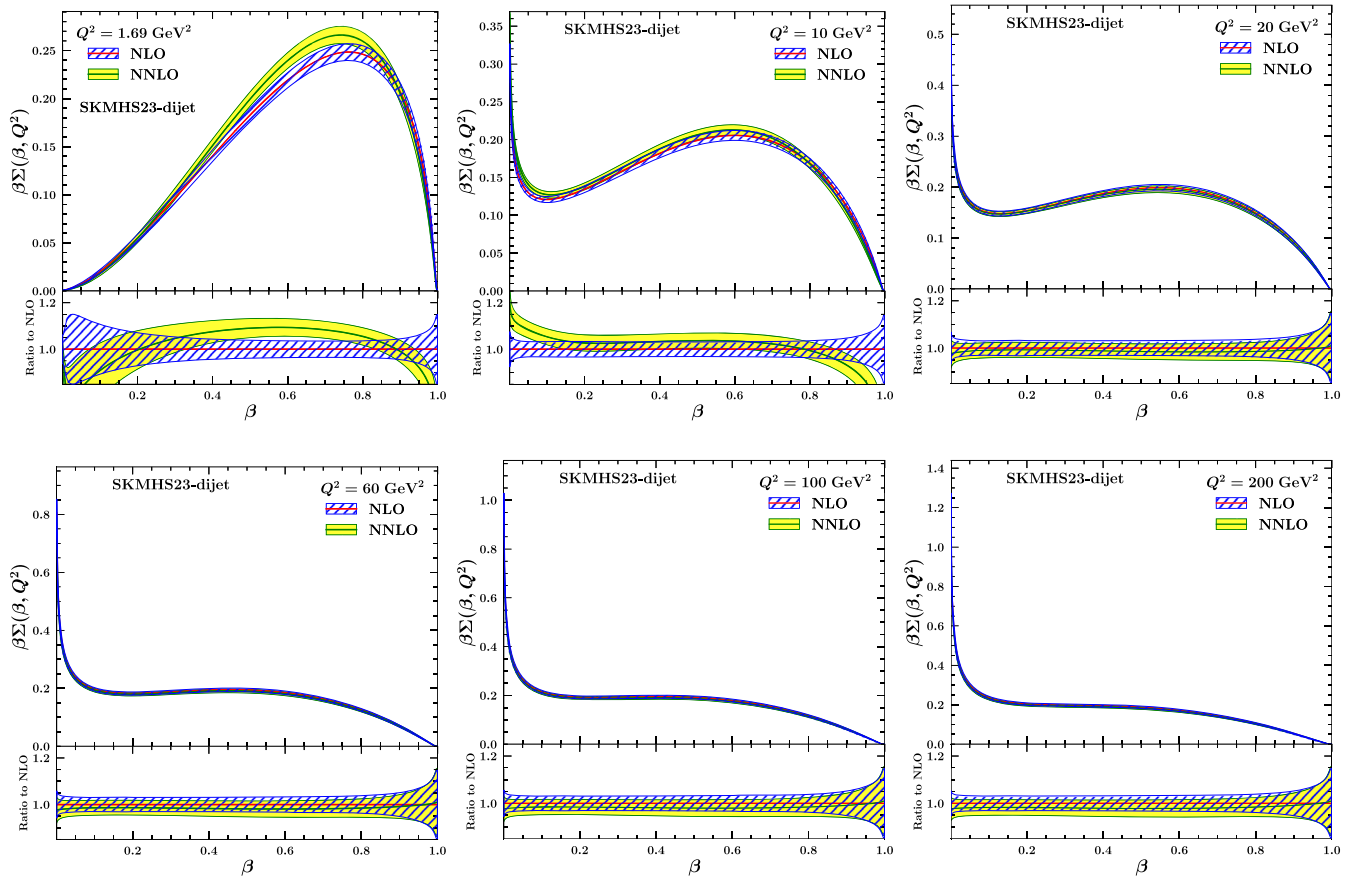

FIG. 5. Same as Fig. 4, but this time for the SKMHS23-dijet singlet distribution with their included uncertainties.

inclusion of the dijet data improves the total χ^2/d.o.f. (degrees of freedom) from 1.11 to 1.09 for our NLO analysis and from 1.10 to 1.07 for the NNLO case. The improvement of the total χ^2 is particularly pronounced when the dijet data are added in the NNLO fit. These findings demonstrate that both the inclusion of the NNLO corrections and considering the dijet data improve the description of the data. These findings are also consistent with the perturbative convergence and the uncertainty estimation discussed above after considering the NNLO accuracy. Concerning the fit quality of the individual experiments, the general trend of the χ^2 per data point is the same as that of the total one for all QCD analyses, with two main exceptions. The χ^2 per data point for the H1-LRG-12, despite remaining good, increases slightly as higher-order QCD corrections are included in the SKMHS23 fit. For the case of H1-LRG-11 $\sqrt{s} = 252$ GeV, this value remains unchanged after inclusion of the NNLO correction in our SKMHS23 fit.

For both SKMHS23 and SKMHS23-dijet analyses, the χ^2 per data point for the case of the H1/ZEUS combined [31] dataset are still large for the NLO and NNLO analysis. This treatment is discussed in detail in Ref. [12]. To decrease the χ^2 for this specific dataset, one needs to impose a minimum cut on the Q^2 value at around 16 GeV^2. In this work, we prefer to consider $Q^2 \geq Q^2_{\text{min}}$ with $Q^2_{\text{min}} = 9$ GeV^2.

We are now in a position to compare our diffractive PDFs to the most recent determinations available in the literature, namely, the GKG18 [12] and our previous work SKMHS22-tw2-tw4-RC [15].

In the analysis by GKG18, they presented the first QCD analysis of diffractive PDFs in the framework of `xFitter` [16], and analyzed for the first time the H1/ZEUS combined datasets [31]. In our most recent work, SKMHS22, we presented a new set of diffractive PDFs and their uncertainties at NLO and NNLO accuracy in perturbative QCD within the `xFitter` framework. The diffractive PDFs have been extracted considering the standard twist-two contribution, the twist-four correction, and the contribution of subleading Reggeon exchange.

Since the GKG18 analysis was performed only at NLO accuracy, we limit the comparison to this order. Such a comparison is shown in Fig. 7 at $Q^2 = 6$ GeV^2 as a function of β, for both gluon and total singlet distributions.

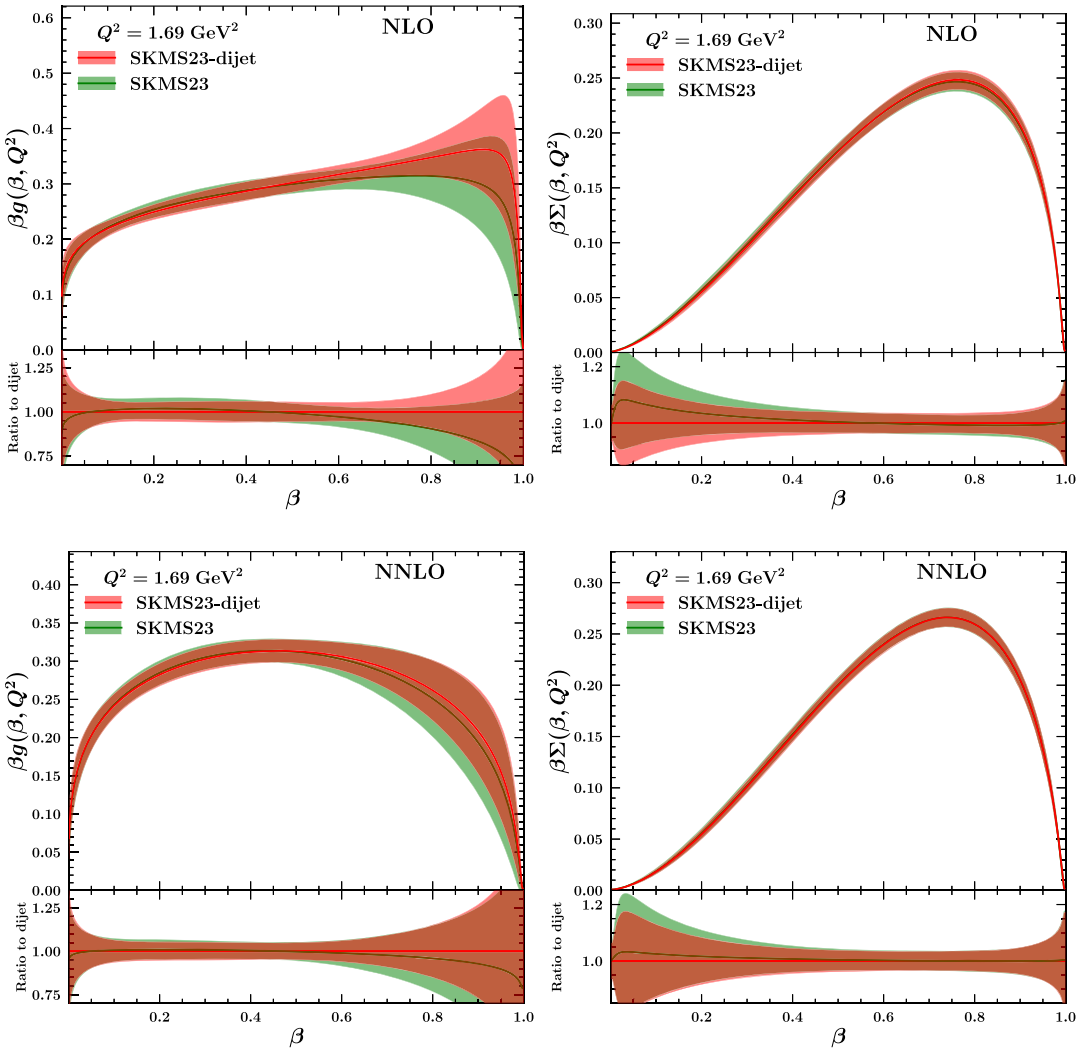

FIG. 6. Comparison of the NLO and NNLO results for the SKMHS23 and SKMHS23-dijet at $Q_0^2 = 1.69$ GeV^2 for the gluon and singlet distributions. The lower panels display the ratio to the SKMHS23-dijet.

TABLE V. The values of χ^2/N_{pts} for both the individual and the total datasets included in the SKMHS23 QCD fit.

		SKMHS23 (NLO)	SKMHS23 (NNLO)
Experiment	Process	χ^2/N_{pts}	χ^2/N_{pts}
H1-LRG-11 $\sqrt{s} = 225$ GeV [29]	Inclusive DDIS	10/13	9/13
H1-LRG-11 $\sqrt{s} = 252$ GeV [29]	Inclusive DDIS	19/12	19/12
H1-LRG-12 [30]	Inclusive DDIS	134/165	136/165
H1/ZEUS combined [31]	Inclusive DDIS	141/96	140/96
χ^2/d.o.f.		308/278 = 1.11	306/278 = 1.10

TABLE VI. The values of χ^2/N_{pts} for both the individual and the total datasets included in the SKMHS23-dijet global QCD fit.

		SKMHS23-dijet (NLO)	SKMHS23-dijet (NNLO)
Experiment	Process	χ^2/N_{pts}	χ^2/N_{pts}
H1-LRG-11 $\sqrt{s} = 225$ GeV [29]	Inclusive DDIS	11/13	10/13
H1-LRG-11 $\sqrt{s} = 252$ GeV [29]	Inclusive DDIS	19/12	18/12
H1-LRG-12 [30]	Inclusive DDIS	135/165	135/165
H1/ZEUS combined [31]	Inclusive DDIS	141/96	139/96
H1-LRG (HERA II) [32]	Inclusive dijet production	12/15	10/15
χ^2/d.o.f.		320/293 = 1.09	314/293 = 1.07

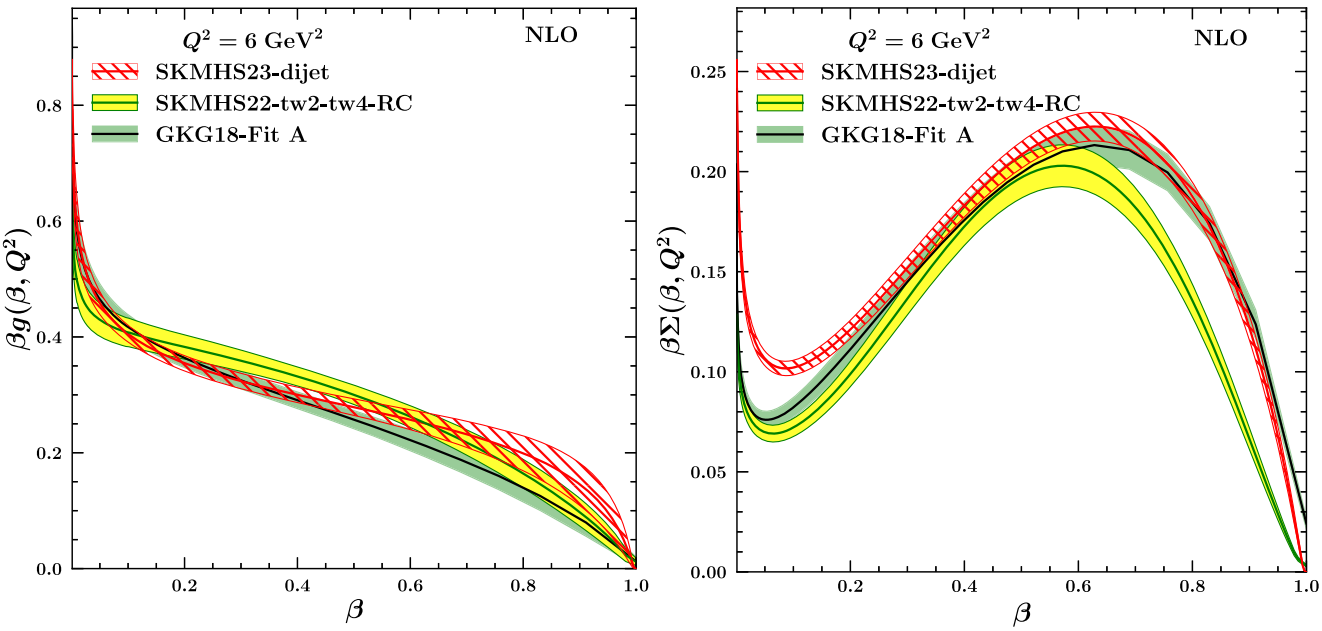

FIG. 7. Comparison between SKMHS23-dijet, GKG18 [12], and SKMHS23 [15] at $Q^2 = 6$ GeV^2 as a function of β, for gluon (left) and total singlet distributions (right).

Concerning the shapes of the diffractive PDFs and their error bands, a number of interesting differences and similarities between these three sets can be seen from the comparisons in Fig. 7. For the case of the gluon density, overall good agreements between these three sets can be seen. However, the new analysis mostly affects the gluon density function over the large value of momentum fraction β. The differences in shape among the three diffractive PDFs sets are more marked in the case of the total singlet. The SKMHS23-dijet analysis is in fairly good agreement with the GKG18 analysis over the medium to large values of β. Both GKG18 and SKMHS22-tw2-tw4-RC are more suppressed at small values of β with respect to the SKMHS23-dijet.

Concerning the diffractive PDF uncertainties, we observe that for both the gluon and total singlet distributions the three sets are in good agreement in the region covered by the high β data, roughly $\beta > 0.4$. Conversely, over the small region of β, differences are more significant. Typically, the uncertainties of the SKMHS23-dijet are smaller than those of both GKG18 and SKMHS22-tw2-tw4-RC.

Furthermore, we now present a comparison of the datasets used in our analysis to the corresponding NNLO theoretical predictions obtained using the NNLO SKMHS23-dijet fit. In Fig. 8 such a comparison is displayed for the NNLO theory prediction calculated using the SKMHS23-dijet global QCD fit with the inclusive diffractive DIS (DDIS) datasets. The comparisons are presented as a function of Q^2 and for four different selected bins of $x_{\mathbb{P}} = 0.001$, 0.003, 0.01, and 0.03, as well as several values of β. The shaded area indicates the experimental uncertainty. As can be seen, in general, an overall very good agreement between the data and the NNLO theoretical predictions is achieved for all diffractive experiments, which is consistent with the χ^2 values per data points reported in Table VI. Remarkably, the SKMHS23-dijet NNLO theoretical predictions and the inclusive diffractive data are in good agreement over the whole kinematical region.

In Fig. 9, we compare the NNLO theory prediction for the inclusive cross section calculated using the SKMHS23-dijet global QCD fit with the H1-LRG-11 $\sqrt{s} = 225$ GeV and H1-LRG-11 $\sqrt{s} = 252$ GeV inclusive diffractive DIS datasets. The NNLO theory prediction is calculated and shown as a function of β and for some selected values of $x_{\mathbb{P}}$ and Q. We show both the absolute distributions (upper panel) and the data/theory ratios (lower panel). As one can see, the theoretical predictions and the data are in good agreement with the H1-LRG-11 $\sqrt{s} = 225$ GeV. A small disagreement with the H1-LRG-11 $\sqrt{s} = 252$ GeV is found which reflects the origin of the large χ^2 reported in Table VI for these data.

Finally, in Fig. 10, we present detailed comparisons between the SKMHS23-dijet NNLO theory predictions with the H1/ZEUS combined data. The comparison are shown as a function of β and for some selected values of Q and $x_{\mathbb{P}}$. The data/theory ratios are also presented in

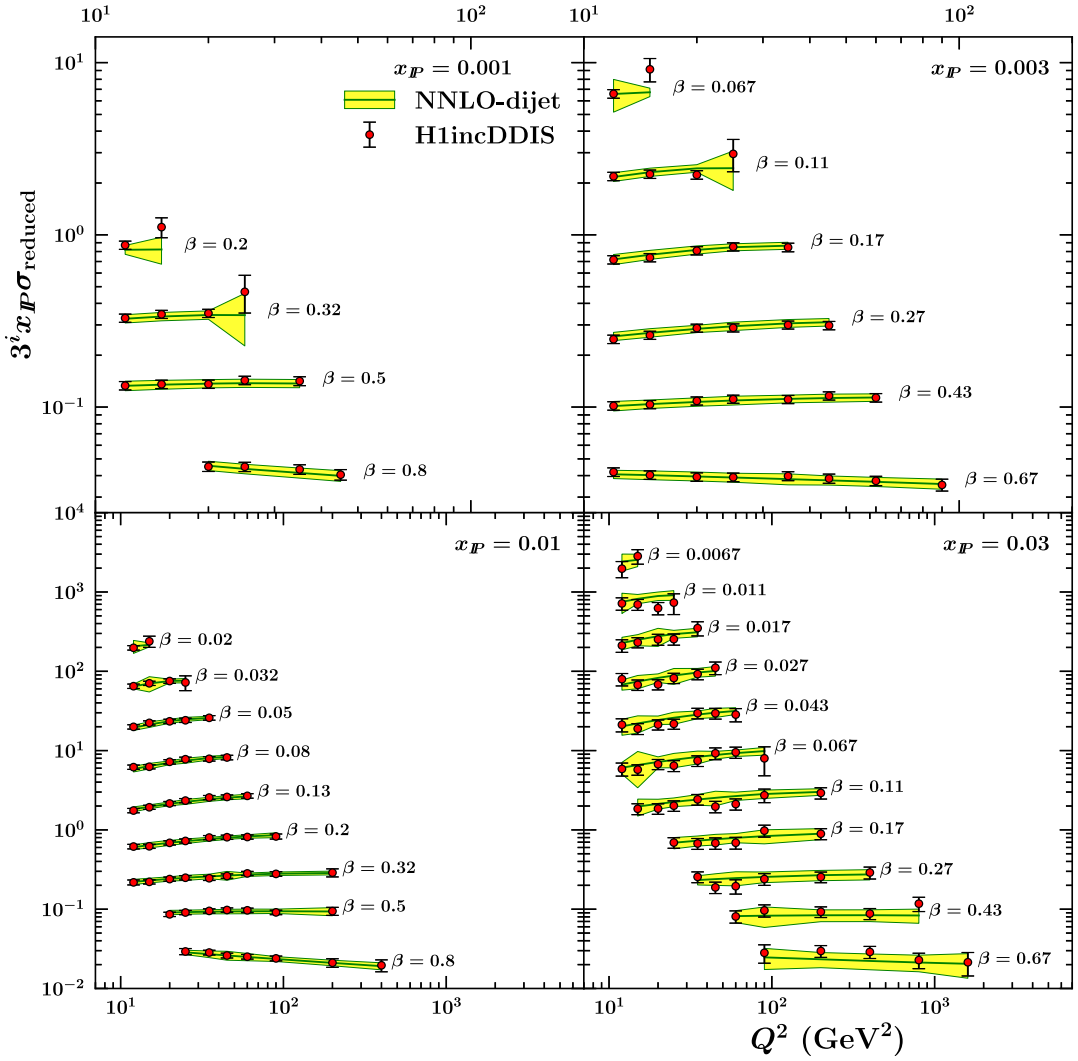

FIG. 8. The NNLO theory prediction obtained using the SKMHS23-dijet global QCD fit in comparison with the inclusive diffractive DIS datasets as a function of Q^2 and for two different selected bins of $x_{\mathbb{P}} = 0.001$, 0.003, 0.01, and 0.03. The shaded area indicates the experimental uncertainty.

the lower panel. Again, an overall good agreement between the data and the SKMHS23-dijet theoretical predictions is achieved over the whole kinematical region.

Now we are in a position to turn our attention to a detailed comparison with the newly added inclusive diffractive dijet production data published by the H1 Collaboration at HERA [31]. In Fig. 11, we compare the NLO and NNLO theory prediction for the diffractive dijet production cross section calculated using the SKMHS23-dijet diffractive PDFs with the diffractive dijet production data. Both the absolute distributions (upper panel) and the data/theory ratios (lower panel) are shown. The comparisons are presented as a function of the transverse momentum p_T and for different values of Q^2 from 4 to 100 GeV^2. In general, a very good agreement between the data and the theoretical predictions is achieved for all values of Q^2. As one can see, the NNLO predictions are very compatible with the data, consistent with the χ^2 values per data points reported in Table VI. For the case of the NLO fit, the $\chi^2/\text{d.o.f.} = 0.80$ is achieved, while for the NNLO fit, we obtained $\chi^2/\text{d.o.f.} = 0.66$. The improvements upon inclusion of the NNLO accuracy is also reflected in the data/theory comparison in Fig. 11 and the smaller error bands in Fig. 6.

V. DISCUSSION AND CONCLUSION

In this work, we have presented SKMHS23 and SKMHS23-dijet, the first determination of diffractive PDFs up to next-to-next-to-leading order accuracy in

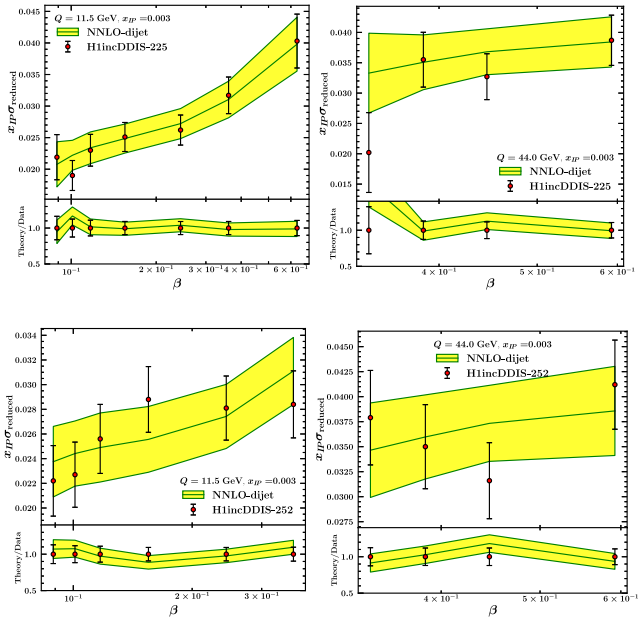

FIG. 9. Comparison of the NNLO theory prediction for the inclusive diffractive cross section obtained using the SKMHS23-dijet with the H1-LRG-11 $\sqrt{s} = 225$ GeV and H1-LRG-11 $\sqrt{s} = 252$ GeV inclusive diffractive DIS datasets. Both the absolute distributions (upper) and the data/theory ratios (lower) are shown.

perturbative QCD taking into account the inclusive DIS and dijet DIS data. The datasets analyzed in this work include the combined H1 HERA-I and HERA-II LRG inclusive diffractive DIS data, H1 low energy HERA-II LRG data, and more importantly the H1 HERA-II dijet LRG data. We have discussed the quality of SKMHS23 and SKMHS23-dijet QCD fits and shown that the inclusion of QCD corrections up to NNLO accuracy improves the description of the data. We have then examined the diffractive PDFs resulting from our QCD fits. We also highlighted their perturbative stability and observed a reduction of the diffractive PDF uncertainties at NNLO with respect to the NLO case. Very good descriptions between the NLO and NNLO predictions based on SKMHS23 and SKMHS23-dijet and the data points are observed over a wide range of $x_{\mathbb{P}}$ and β. The extracted diffractive PDFs are also compared with the results available in the literature, where largely good agreement is found.

In our SKMHS23 and SKMHS23-dijet analysis we have introduced some methodological improvements, and the theoretical framework applied in this work also features a number of further improvements. As we discussed, a well-established fitting methodology is used to provide a faithful representation of the diffractive experimental uncertainties,

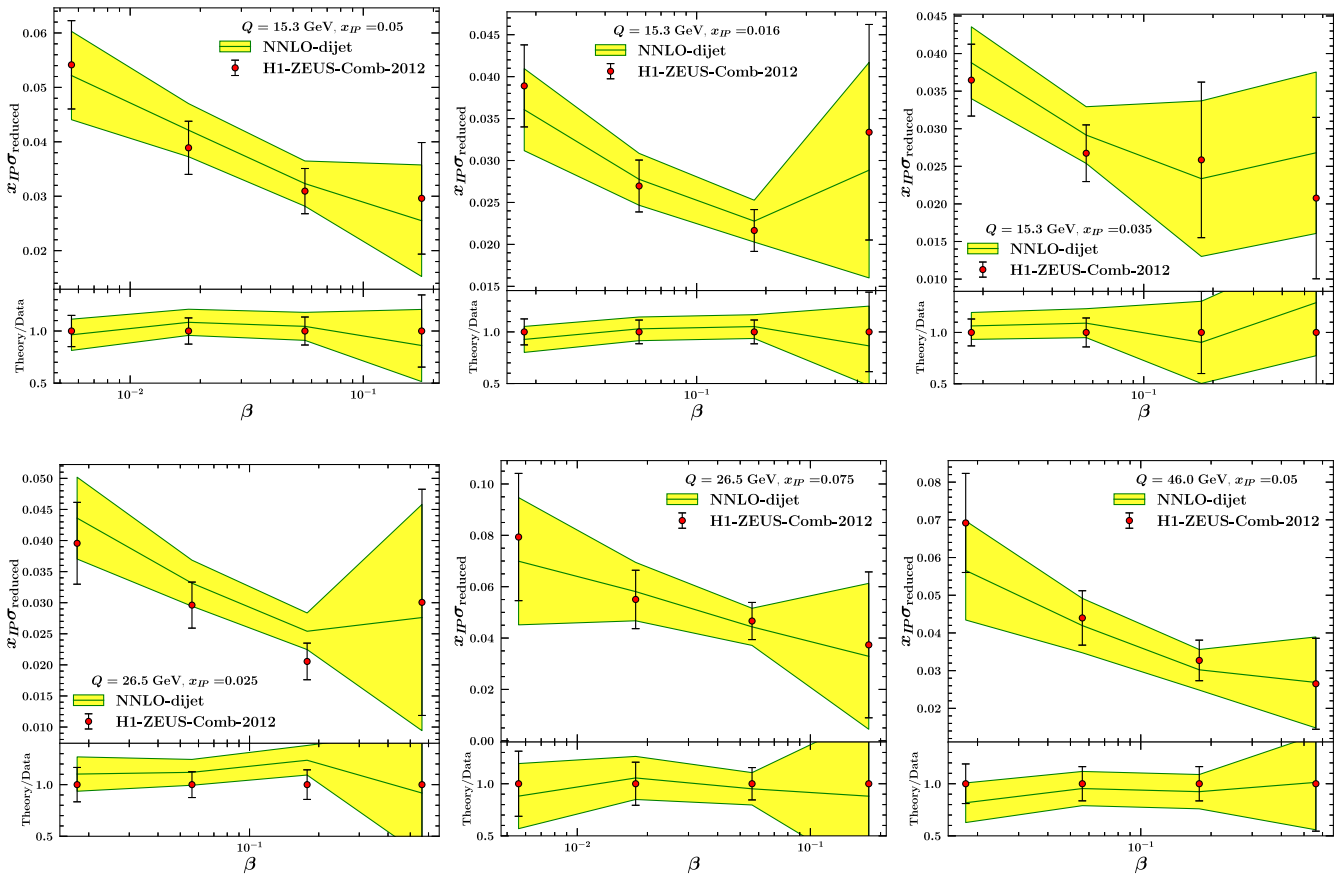

FIG. 10. Same as Fig. 9, but this time in comparison with the H1/ZEUS combined data.

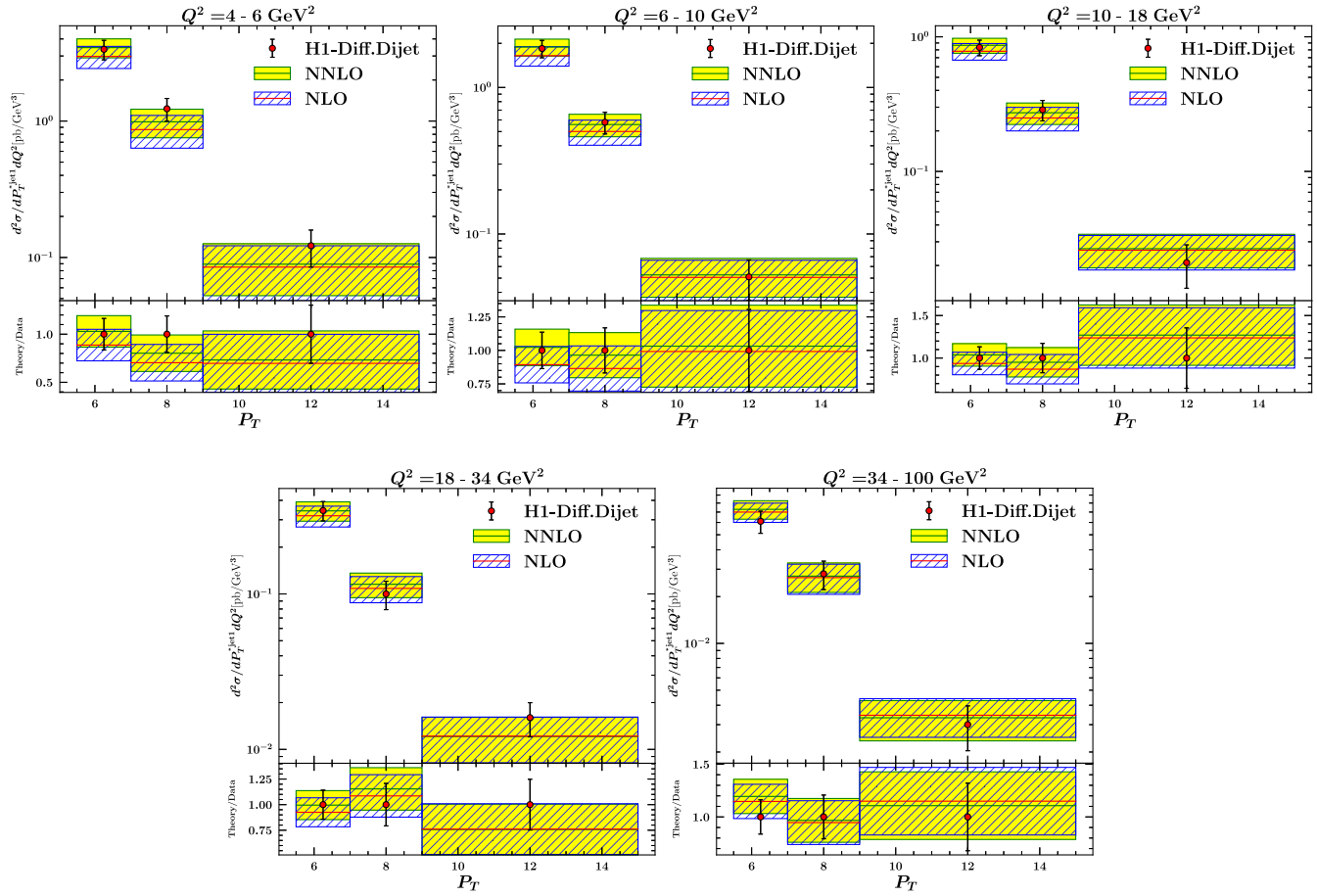

FIG. 11. Comparison of the NLO and NNLO theory prediction for diffractive dijet production cross section calculated using the SKMHS23-dijet diffractive PDFs with the diffractive dijet production data published by the H1 Collaboration at HERA [31]. Both the absolute distributions (upper) and the data/theory ratios (lower) are shown as well.

and to minimize any bias related to the parametrization of the diffractive PDFs and to the minimization of the fitting procedure.

The theoretical calculations have been done at NLO and NNLO accuracy for both inclusive and jet production using the APFEL and fastNLO schemes, as well as ALPOS to perform the PDF fit. To consider the contribution from heavy quarks, we employed the FONLL-B and FONLL-C GM-VFNS approaches which provide a proper theory input for such contributions at NLO and NNLO accuracy, respectively.

The H1 HERA-II dijet LRG data are also added to the data sample to constrain the gluon component which is weekly constrained from the inclusive diffractive DIS data. Hence, we expect that the determination of the gluon distribution is more reliable in our SKMHS23-dijet QCD fit, since the dijets from HERA-II are considered, which are directly sensitive to the gluon density.

The SKMHS23 and SKMHS23-dijet analyses presented in this work represent the first step of a broader program. A number of updates and improvements are foreseen, and the SKMHS23 and SKMHS23-dijet analyses presented in this article can be extended in several different directions. The most important one is to repeat the analysis described here and present a new combined QCD analysis of both recent datasets measured by the H1 and ZEUS Collaborations at HERA, and the expected observables from the future colliders considering the large hadron-electron collider [48] on the top of the list, to examine the effect of such data on the extracted diffractive PDFs.

The SKMHS23 and SKMHS23-dijet NLO and NNLO diffractive PDF sets presented in this work are available in the standard LHAPDF format [49] from the authors upon request.

ACKNOWLEDGMENTS

H. K., H. H., and M. Soleymaninia thank the School of Particles and Accelerators, Institute for Research in Fundamental Sciences (IPM) for financial support of this project. H. K. also is thankful to the Physics Department of University of Udine, and the University of Science and Technology of Mazandaran for the financial support

provided for this research. M. Soleymaninia is thankful to the Iran Science Elites Federation for the financial support. This work was also supported in part by the Deutsche Forschungsgemeinschaft (DFG, German Research Foundation) through the funds provided to the Sino-German Collaborative Research Center TRR110 "Symmetries and the Emergence of Structure in QCD" (DFG Project-ID 196253076—TRR 110). The work of U.-G. M. was supported in part by the Chinese Academy of Sciences (CAS) President's International Fellowship Initiative (PIFI) (Grant No. 2018DM0034) and by VolkswagenStiftung (Grant No. 93562).

[1] S. Chekanov *et al.* (ZEUS Collaboration), Deep inelastic scattering with leading protons or large rapidity gaps at HERA, Nucl. Phys. **B816**, 1 (2009).
[2] L. Frankfurt, V. Guzey, A. Stasto, and M. Strikman, Selected topics in diffraction with protons and nuclei: Past, present, and future, Rep. Prog. Phys. **85**, 126301 (2022).
[3] A. Aktas *et al.* (H1 Collaboration), Diffractive open charm production in deep-inelastic scattering and photoproduction at HERA, Eur. Phys. J. C **50**, 1 (2007).
[4] A. Aktas *et al.* (H1 Collaboration), Measurement and QCD analysis of the diffractive deep-inelastic scattering cross-section at HERA, Eur. Phys. J. C **48**, 715 (2006).
[5] S. Chekanov *et al.* (ZEUS Collaboration), A QCD analysis of ZEUS diffractive data, Nucl. Phys. **B831**, 1 (2010).
[6] J. C. Collins, D. E. Soper, and G. F. Sterman, Factorization of hard processes in QCD, Adv. Ser. Dir. High Energy Phys. **5**, 1 (1989).
[7] J. C. Collins, Proof of factorization for diffractive hard scattering, Phys. Rev. D **57**, 3051 (1998); **61**, 019902(E) (2000).
[8] Y. L. Dokshitzer, Calculation of the structure functions for deep inelastic scattering and e+ e- annihilation by perturbation theory in quantum chromodynamics, Sov. Phys. JETP **46**, 641 (1977).
[9] V. N. Gribov and L. N. Lipatov, Deep inelastic e p scattering in perturbation theory, Sov. J. Nucl. Phys. **15**, 438 (1972).
[10] L. N. Lipatov, The parton model and perturbation theory, Yad. Fiz. **20**, 181 (1974).
[11] G. Altarelli and G. Parisi, Asymptotic freedom in parton language, Nucl. Phys. **B126**, 298 (1977).
[12] M. Goharipour, H. Khanpour, and V. Guzey, First global next-to-leading order determination of diffractive parton distribution functions and their uncertainties within the `xFitter` framework, Eur. Phys. J. C **78**, 309 (2018).
[13] H. Khanpour, Phenomenology of diffractive DIS in the framework of fracture functions and determination of diffractive parton distribution functions, Phys. Rev. D **99**, 054007 (2019).
[14] A. Maktoubian, H. Mehraban, H. Khanpour, and M. Goharipour, Role of higher twist effects in diffractive DIS and determination of diffractive parton distribution functions, Phys. Rev. D **100**, 054020 (2019).
[15] M. Salajegheh, H. Khanpour, U.-G. Meißner, H. Hashamipour, and M. Soleymaninia, Global QCD analysis of diffractive parton distribution function considering higher twist corrections within the xFitter framework, Phys. Rev. D **106**054012 (2022).
[16] S. Alekhin, O. Behnke, P. Belov, S. Borroni, M. Botje, D. Britzger, S. Camarda, A. M. Cooper-Sarkar, K. Daum, C. Diaconu *et al.*, HERAFitter, Eur. Phys. J. C **75**, 304 (2015); H. Abdolmaleki *et al.* (xFitter Developers' Team), xFitter: An open source QCD analysis framework. A resource and reference document for the Snowmass study, arXiv:2206.12465.
[17] D. Britzger, J. Currie, T. Gehrmann, A. Huss, J. Niehues, and R. Žlebčík, Dijet production in diffractive deep-inelastic scattering in next-to-next-to-leading order QCD, Eur. Phys. J. C **78**, 538 (2018).
[18] D. Britzger, C. Ewerz, S. Glazov, O. Nachtmann, and S. Schmitt, The tensor pomeron and low-x deep inelastic scattering, Phys. Rev. D **100**, 114007 (2019).
[19] https://indico.desy.de/event/22011/contributions/44932/.
[20] D. Britzger *et al.*, The ALPOS fit framework, available at http://www.desy.de/britzger/alpos/.
[21] V. Bertone, S. Carrazza, and J. Rojo, APFEL: A PDF evolution library with QED corrections, Comput. Phys. Commun. **185**, 1647 (2014).
[22] D. Britzger *et al.* (fastNLO Collaboration), New features in version 2 of the fastNLO project, arXiv:1208.3641.
[23] M. Wobisch *et al.* (fastNLO Collaboration), Theory-data comparisons for jet measurements in hadron-induced processes, arXiv:1109.1310.
[24] J. Currie, T. Gehrmann, and J. Niehues, Precise QCD Predictions for the Production of Dijet Final States in Deep Inelastic Scattering, Phys. Rev. Lett. **117**, 042001 (2016).
[25] J. Currie, T. Gehrmann, A. Huss, and J. Niehues, NNLO QCD corrections to jet production in deep inelastic scattering, J. High Energy Phys. 07 (2017) 018; 12 (2020) 042.
[26] Z. Nagy and Z. Trocsanyi, Multijet Cross-Sections in Deep Inelastic Scattering at Next-to-Leading Order, Phys. Rev. Lett. **87**, 082001 (2001).
[27] T. Gehrmann, X. Chen, J. Cruz-Martinez, J. R. Currie, E. W. N. Glover, T. A. Morgan, J. Niehues, D. M. Walker, R. Gauld, A. Gehrmann-De Ridder *et al.*, Jet cross sections and transverse momentum distributions with NNLOJET, Proc. Sci. RADCOR2017 (**2018**) 074.
[28] D. A. Britzger, Regularized unfolding of jet cross sections in deep-inelastic ep scattering at HERA and determination of the strong coupling constant, Ph.D. thesis, 10.3204/DESY-THESIS-2013-045.
[29] F. D. Aaron *et al.* (H1 Collaboration), Measurement of the diffractive longitudinal structure function F_L^D at HERA, Eur. Phys. J. C **71**, 1836 (2011).

[30] F. D. Aaron *et al.* (H1 Collaboration), Inclusive measurement of diffractive deep-inelastic scattering at HERA, Eur. Phys. J. C **72**, 2074 (2012).
[31] F. D. Aaron *et al.* (H1 and ZEUS Collaborations), Combined inclusive diffractive cross sections measured with forward proton spectrometers in deep inelastic ep scattering at HERA, Eur. Phys. J. C **72**, 2175 (2012).
[32] V. Andreev *et al.* (H1 Collaboration), Measurement of dijet production in diffractive deep-inelastic ep scattering at HERA, J. High Energy Phys. 03 (2015) 092.
[33] F. D. Aaron *et al.* (H1 Collaboration), Measurement of dijet production in diffractive deep-inelastic scattering with a leading proton at HERA, Eur. Phys. J. C **72**, 1970 (2012).
[34] V. Andreev *et al.* (H1 Collaboration), Diffractive dijet production with a leading proton in ep collisions at HERA, J. High Energy Phys. 05 (2015) 056.
[35] A. Aktas *et al.* (H1 Collaboration), Tests of QCD factorisation in the diffractive production of dijets in deep-inelastic scattering and photoproduction at HERA, Eur. Phys. J. C **51**, 549 (2007).
[36] S. Chekanov *et al.* (ZEUS Collaboration), Dijet production in diffractive deep inelastic scattering at HERA, Eur. Phys. J. C **52**, 813 (2007).
[37] A. Aktas *et al.* (H1 Collaboration), Dijet cross sections and parton densities in diffractive DIS at HERA, J. High Energy Phys. 10 (2007) 042.
[38] F. D. Aaron, C. Alexa, V. Andreev, S. Backovic, A. Baghdasaryan, E. Barrelet, W. Bartel, K. Begzsuren, A. Belousov, J. C. Bizot *et al.*, Measurement of the cross section for diffractive deep-inelastic scattering with a leading proton at HERA, Eur. Phys. J. C **71**, 1578 (2011).
[39] M. Tanabashi *et al.* (Particle Data Group), Review of particle physics, Phys. Rev. D **98**, 030001 (2018).
[40] M. Cacciari, M. Greco, and P. Nason, The P(T) spectrum in heavy flavor hadroproduction, J. High Energy Phys. 05 (1998) 007.
[41] S. Forte, E. Laenen, P. Nason, and J. Rojo, Heavy quarks in deep-inelastic scattering, Nucl. Phys. **B834**, 116 (2010).
[42] S. Forte, D. Napoletano, and M. Ubiali, Higgs production in bottom-quark fusion in a matched scheme, Phys. Lett. B **751**, 331 (2015).
[43] R. D. Ball *et al.* (NNPDF Collaboration), Parton distributions for the LHC Run II, J. High Energy Phys. 04 (2015) 040.
[44] V. Bertone, Higher order and heavy quark mass effects in the determination of parton distribution functions, nnpdf.mi.infn.it/wp-content/uploads/2017/10/VBertone-thesis.pdf.
[45] V. Andreev *et al.* (H1 Collaboration), Measurement of multijet production in ep collisions at high Q^2 and determination of the strong coupling α_s, Eur. Phys. J. C **75**, 65 (2015).
[46] F. James and M. Roos, MINUIT: A system for function minimization and analysis of the parameter errors and correlations, Comput. Phys. Commun. **10**, 343 (1975).
[47] P. M. Nadolsky, H. L. Lai, Q. H. Cao, J. Huston, J. Pumplin, D. Stump, W. K. Tung, and C. P. Yuan, Implications of CTEQ global analysis for collider observables, Phys. Rev. D **78**, 013004 (2008).
[48] P. Agostini *et al.* (LHeC and FCC-he Study Group), The large hadron–electron collider at the HL-LHC, J. Phys. G **48**, 110501 (2021).
[49] A. Buckley, J. Ferrando, S. Lloyd, K. Nordström, B. Page, M. Rüfenacht, M. Schönherr, and G. Watt, LHAPDF6: Parton density access in the LHC precision era, Eur. Phys. J. C **75**, 132 (2015).